Surface-micromachined magnetic undulator with period length between 10 μm and 1 mm for advanced light sources

Jere Harrison,* Abhijeet Joshi,† Jonathan Lake,‡ and Rob Candler§

Department of Electrical Engineering, University of California, Los Angeles, Los Angeles, California 90095-1594, USA

Pietro Musumeci‖

Department of Physics, University of California, Los Angeles, Los Angeles, California 90095-1594, USA

(Received 24 November 2011; published 31 July 2012)

A technological gap exists between the μm-scale wiggling periods achieved using electromagnetic waves of high intensity laser pulses and the mm scale of permanent-magnet and superconducting undulators. In the sub-mm range, surface-micromachined soft-magnetic micro-electro-mechanical system inductors with integrated solenoidal coils have already experimentally demonstrated 100 to 500 mT field amplitude across air gaps as large as 15 μm. Simulations indicate that magnetic fields as large as 1.5 T across 50 μm inductor gaps are feasible. A simple rearranging of the yoke and pole geometry allows for fabrication of 10+ cm long undulator structures with period lengths between 12.5 μm and 1 mm. Such undulators find application both in high average power spontaneous emission sources and, if used in combination with ultrahigh-brightness electron beams, could lead to the realization of low energy compact free-electron lasers. Challenges include electron energy broadening due to wakefields and Joule heating in the electromagnet.

DOI: 10.1103/PhysRevSTAB.15.070703 PACS numbers: 41.60.−m, 85.70.−w

I. BACKGROUND

Undulator and wiggler magnets play a key role in the development of modern x-ray sources. The output spectrum of the radiation generated by the passage of relativistic particles in a planar oscillating magnetic field peaks at the resonant wavelength λ_r,

$$\lambda_r \cong \frac{\lambda_u(1 + K^2/2)}{2\gamma^2}, \tag{1}$$

where λ_u is the undulator period, K is the normalized rms undulator vector potential, and γ the electron Lorentz factor.

Conventional undulator technology uses permanent magnet and steel-yoke or superconducting electromagnetic undulators with period $\lambda_u > 1$ mm. To access the x-ray region of the electromagnetic spectrum and generate radiation at a wavelength $\lambda_r = 1$ nm with these period lengths, a minimum beam energy of 500 MeV ($\gamma \sim 1000$) is required.

*jere.harrison@ucla.edu
†abhijeet@ucla.edu
‡jonathan.lake@ucla.edu
§rcandler@ee.ucla.edu
‖musumeci@physics.ucla.edu

Undulators with period range between 10 μm and 1 mm could be very interesting as they would enable access to the short wavelength region of the electromagnetic spectrum with modest energy electron beams. These devices could take advantage of the continuous progress in the generation of ultrahigh-brightness electron beams and would constitute an attractive solution for lowering the energy and cost requirements of electron accelerators for next generation free-electron laser (FEL)-based x-ray sources [1]. At the same time, microundulators would also constitute a valid alternative to inverse Compton scattering (ICS) [2] sources, as short wiggling periods and long interaction lengths could be obtained without the use of high power laser systems.

Undulator designs with period lengths in the mm to sub-mm range date back to the mid-1980's. Granatstein proposed a design for mm-scale pulsed electromagnetic undulators [3]. Ramian proposed using periodic grooves ground into samarium cobalt blocks to produce a mm-scale undulating field [4]. Paulson built and characterized this undulator design, demonstrating that machined permanent magnets could be used to reduce the period length to 4 mm. His work noted the unsolved drawbacks of smaller magnetic fields, DC and long-period field errors, and large end fields [5]. Paulson proposed integrated electromagnets and magnetic end caps as potential solutions, but this was not pursued further at the time due to the expected manufacturing complexities. Tatchyn *et al.* proposed and fabricated hybrid-bias-permanent-magnet undulators with period lengths in the range of $\lambda_u = 700$–800 μm. Magnetic testing of these ''micropole'' undulators showed fields as high

as 0.38 T [6]. These undulators successfully demonstrated 960 fW of 66 eV soft x-ray/VUV radiation from a 70 MeV 1 nA linear accelerator at Lawrence Livermore National Laboratory [7]. The magnetic field in these devices was limited by the low remnant field of the NbFeB permanent magnets (0.73 T) and by the 200+ μm gap required to accommodate the electron beam. Electron-beam size, positioning, and stability were identified as primary limitations on further developing the technology. Another limitation was identified in the transverse and longitudinal disturbances to the electron-beam energy by wakefields within the undulator [8]. In subsequent years, the emittance and stability of electron beams have improved by orders of magnitude [9].

Since these early efforts, the range of undulator period lengths between 10 and 700 μm has remained inaccessible. Laser undulators at these wavelengths are limited by a lack of high intensity gain media. Permanent magnets, on the other hand, are limited by crystal grain and magnetic domain size limits [10]. Machining technology does not exist to manufacture superconducting undulators with sub-mm period, and the only other feasible alternative, "slow light" cavity undulators, have yet to be experimentally demonstrated [11].

Recent progress on surface-micromachined magnetic materials [12,13] and devices [14–16] has enabled soft-magnet inductors and actuators to be fabricated by photolithography and electroforming with precision on the range of a few μm in the lateral dimensions and film thicknesses in excess of 50 μm. These surface-micromachined inductors produce 80 to 400 kA/m magnetic fields across air gaps up to 15 μm.

In this paper we explore the possibility of adopting the progress in micromachining magnetic materials and devices to the development of undulators with period lengths between 10 μm and 1 mm (Fig. 1). We will consider as examples undulators with periods of $\lambda_u = 100$ μm and $\lambda_u = 400$ μm which have gaps large enough to fit existing sub-mm-mrad emittance electron beams. In particular, we analyze the possibility of using microundulators with $\lambda_u = 100$ μm for producing high-average-power high-energy undulator radiation, and of $\lambda_u = 400$ μm undulators for FEL amplification. Period lengths shorter than 100 μm will require active cooling to accommodate the increased current density in the coil, and gaps smaller than 50 μm will require smaller electron-beam emittance than is presently available and new strategies to mitigate the energy modulation caused by wakefields.

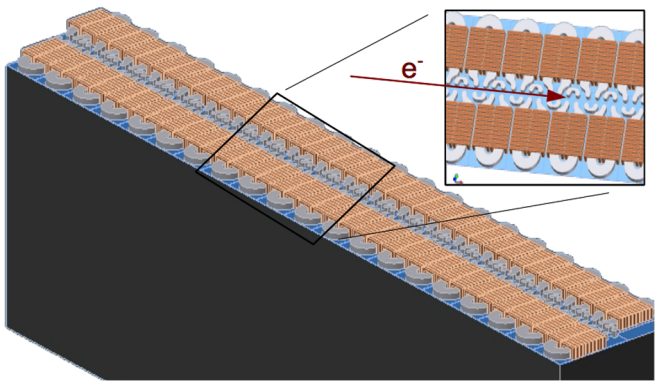

FIG. 1. CAD rendering of a potential microundulator design on a 500 μm thick silicon substrate.

In the first part of the paper we discuss design optimization decisions and describe the microfabrication processes required for the construction of these novel undulators. The mature process technologies used for these devices can provide high-aspect-ratio (> 100:1 sidewall slope) thick (10 μm–100 μm) electroformed magnetic films, creating fields across transverse cross sections that are large enough to accommodate currently available electron beams. The actively powered nature of these devices also enables the dynamic manipulation of the undulator magnetic field by modulating the driving current. This rapid ($\tau = 10$ ns–10 μs) tuning of the undulator field facilitates modulation of the light beam, automated tuning of the field uniformity, and arbitrary field strength tapering of the undulator. In the second part of the paper, we investigate topics concerning the operation of short-period electromagnetic undulators within a beam line. The heat dissipation of the electromagnet and electron-beam induced currents in the beam pipe, sensitivity of the electromagnets to external magnetic fields, and wakefield modulation of electron energy will be explored. In the third part of the paper, we give two application examples where such a short period undulator could be employed: a spontaneous emission source based on a high average current electron source and an FEL amplifier driven by an ultrahigh-brightness beam. In the last section of the paper, we present a road map of an experiment in the visible spectral range for testing a prototype at the UCLA Pegasus photoinjector laboratory.

II. SOFT-MAGNET UNDULATOR DESIGN

Soft-magnet undulators require an actively powered coil producing magnetomotive force (MMF) to generate magnetic flux, a magnetic yoke to direct the flux across the undulator gap, and engineered magnetic pole tips to concentrate the magnetic flux density. The maximum field that can be generated is limited by the saturation magnetization of the magnetic yoke, which is as high as 2.1 T for electroplated alloys of CoNiFe [13] and CoNiP. Another limitation comes from the magnetic flux that fringes across the yoke before reaching the undulator gap. Peak flux densities may range from 100 mT to over 1 T in the gap, depending on the design. The undulator period length is limited at a lower bound by the resolution of the thick photoresist mold that is used in the magnetic yoke fabrication process, typically ~10 μm, and at an upper bound by the size of the silicon wafer used in fabrication, typically 100 mm in a university cleanroom and 300 mm in a commercial cleanroom.

Several obstacles have prevented soft-magnet micro-electro-mechanical system (MEMS) devices from achieving widespread use. The complex fabrication process required to produce integrated 3D coils has limited nearly all previous devices to inefficient planar coils or external magnetic flux sources, two options that would prevent the scaling of microfabricated undulator period length to the sub-mm level. Depositing high-quality magnetic films thicker than 10 μm requires expertise in electrochemistry and controlled atmosphere tools, a significant barrier to entry in the field. Additionally, the microfabrication requires an assortment of cleanroom fabrication tools and significant experience. Thick magnetic film devices, in particular, use atypical processes such as thick photoresist electroplating molds and photolithography over high aspect-ratio topology.

A. Magnetic flux generation

The ''racetrack'' solenoidal coil is an area-efficient design that fits the windings and yoke into a long and narrow space, ideal for short period undulators (Fig. 2). The solenoidal coil design can fit an order of magnitude or more windings into a given surface area than the simpler and more common planar MEMS coil design.

For a single electromagnetic undulator period with a high permeability magnetic yoke, the fraction of generated magnetic flux that is channeled into the undulator gap is a function of the reluctance of the magnetic path across the gap relative to the magnetic reluctance of all other return paths in parallel. Careful design of the flux path is required to minimize the reluctance of the desired path and maximize the reluctance of all other paths.

It is possible to generate the magnetic flux on one side of the undulator (Design 1) or on both sides of the undulator axis as in a typical electromagnetic undulator (Design 2) [17], as shown in Fig. 3. Directing the flux through MMF sources located only on one side of the undulator axis to a short yoke on the other side (Design 1) allows doubling the

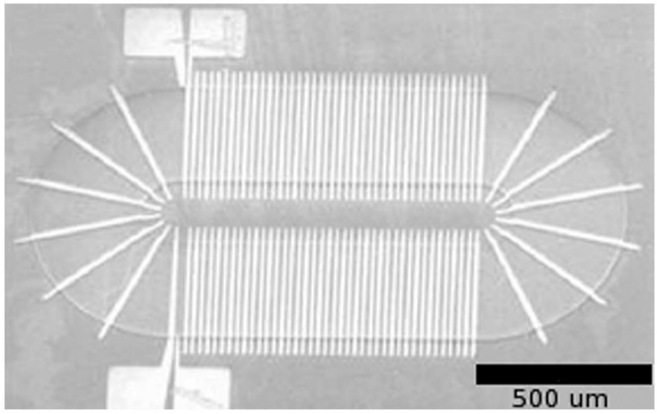

FIG. 2. Scanning electron micrograph of a surface-micromachined racetrack transformer fabricated at UCLA.

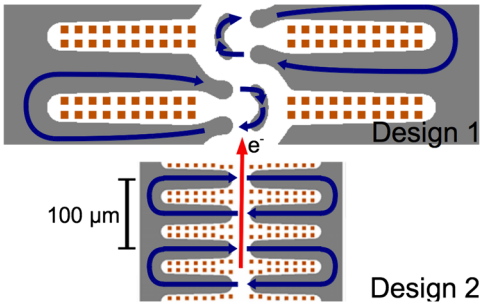

FIG. 3. Illustration of a two period cross section of two undulator designs with $\lambda_u = 100$ μm. Design 1 allows further scaling. The magnetic yoke is shown in gray, the solenoid winding interconnect cross sections are shown in orange, and the intended magnetic flux path is shown in blue.

yoke width and spacing for a given undulator period length, but at the cost of additional parasitic magnetic fringing between the short yokes. As a result, directing the flux through MMF sources on both sides of the undulator axis (Design 2) achieves a larger peak magnetic field but also a longer minimum manufacturable period length.

The undulator period and gap are primarily limited by three effects during manufacturing, diffraction, uneven absorption during photolithography, and high internal stress in the photoresist electroplating molds.

The diffraction limited critical dimension for photolithography, where adjacent lines and spaces follow precisely from the mask pattern, is expressed by

$$b_{\mathrm{crit}} = \frac{3}{2}\sqrt{\frac{\lambda_l z}{2}}, \tag{2}$$

where b_{crit} is the feature width that can be precisely resolved, λ_l is the wavelength of the photolithography light source, and z is the thickness of the photoresist [18]. For the 100 μm thick photoresist electroplating mold proposed for the electromagnet yoke exposed with an i-line (365 nm) mercury arc-vapor lamp, experimental results [19] confirm the simple estimates based on Eq. (2) and yield a limit between 5 and 10 μm. Thick chemically amplified photoresists have experimentally demonstrated 7 μm lateral features in 100 μm thick SU8-10 [19], 15 μm lateral features in 1.5 mm thick SU8-2150 [20], and 18 μm lateral features in 180 μm thick KMPR [21].

The resolution limitations imposed by internal stress in the photoresist can be significantly coarser than the effects of diffraction and dose absorption in negative-tone thick-film photoresists. For some geometries, the internal stress of the negative-tone photoresist electroforming mold used during fabrication of the undulator yoke and windings will exceed the adhesion strength between the mold and the preceding film. Fabrication test structures have shown electroplating mold failure for length-to-width ratios less than 4 to 1 for 50 μm thick films. With a yoke length equal to the undulator period, the spacing between magnetic

yokes is limited to 12.5 μm for a 50 μm thick yoke given the limitation stated above. This limits Design 1 to undulator periods greater than 12.5 μm and Design 2 to undulator periods greater than 25 μm. Scaling beyond these limitations may be achieved if new high-resolution thick-film photoresists are developed with lower internal stress.

B. Managing the field

The achievable peak magnetic flux density and uniformity is governed by the geometry of the flux source. Different geometric designs can be analyzed using Hopkinson's/Rowland's magnetic analogy to Ohm's law,

$$\phi = \frac{\mathcal{F}}{\mathcal{R}_{\text{total}}}, \tag{3}$$

where ϕ is the total magnetic flux, $\mathcal{F}$ is the MMF, and $\mathcal{R}_{\text{total}}$ is the total reluctance of all flux paths. The reluctance of a flux path is

$$\mathcal{R} = \frac{L}{\mu T W}, \tag{4}$$

where L is the flux path length, μ is the permeability, T is the yoke thickness, and W is the yoke width. Reluctances in parallel add like electrical resistors in parallel ($\mathcal{R}^{-1}_{\text{parallel}} = \mathcal{R}_1^{-1} + \mathcal{R}_2^{-1}$), while reluctances in series add like resistors in series ($\mathcal{R}_{\text{series}} = \mathcal{R}_1 + \mathcal{R}_2$). The total magnetic flux delivered to the undulator gap will be reduced by the fringing flux paths in parallel with the desired flux path in the system. Figure 4 shows a reluctance model of the undulator neglecting 3D fringing and period-to-period fringing. For undulators with the yoke of each period unconnected to the next, period-to-period fringing is negligible. For yoke geometries with cross sectional thickness (T_y) within a factor of 4 of the width (W_y), finite element method (FEM) simulations show that parasitic

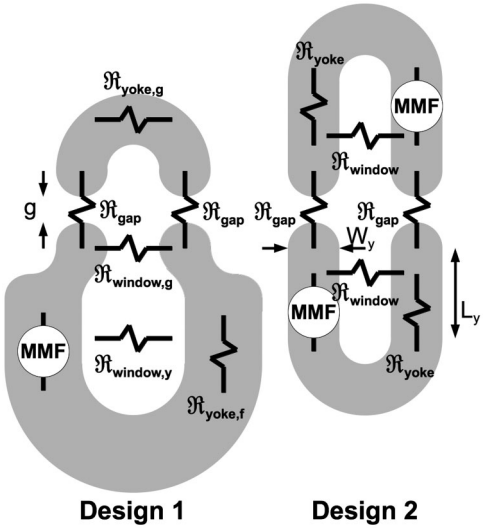

FIG. 4. Illustration of a simple reluctance model of the two undulator designs illustrated in Fig. 3.

3D fringing will reduce the peak field by 5%–10% from this model.

The equations for the total, fringing, and return flux path reluctances can be obtained from Fig. 4 and are shown below with numbered subscripts distinguishing between designs:

$$\mathcal{R}_{\text{total, 1}} = \mathcal{R}_{\text{yoke, }f} + (\mathcal{R}^{-1}_{\text{fringe, 1}} + \mathcal{R}^{-1}_{\text{return, 1}})^{-1}$$
$$\mathcal{R}_{\text{fringe, 1}} = (\mathcal{R}^{-1}_{\text{window, }y} + \mathcal{R}^{-1}_{\text{window, }g})^{-1}$$
$$\mathcal{R}_{\text{return, 1}} = 2\mathcal{R}_{\text{gap}} + \mathcal{R}_{\text{yoke, }g}$$
$$\mathcal{R}_{\text{total, 2}} = \mathcal{R}_{\text{yoke, }f} + (\mathcal{R}^{-1}_{\text{fringe, 2}} + \mathcal{R}^{-1}_{\text{return, 2}})^{-1}$$
$$\mathcal{R}_{\text{fringe, 2}} = \mathcal{R}_{\text{window}}$$
$$\mathcal{R}_{\text{return, 2}} = 2\mathcal{R}_{\text{gap}} + (\mathcal{R}^{-1}_{\text{yoke}} + \mathcal{R}^{-1}_{\text{window}})^{-1}.$$

Magnetic saturation sets the upper bound for efficient generation of magnetic flux in the undulator yoke. The magnetic flux density in the yoke is

$$B_{\text{yoke}} = \frac{\phi_{\text{total}}}{W_y T_y}. \tag{5}$$

Magnetic circuit analysis shows that the flux remaining at the magnetic pole tips is

$$\phi_{\text{tip}} = \frac{\phi_{\text{total}}}{1 + \mathcal{R}_{\text{return}}/\mathcal{R}_{\text{fringe}}}. \tag{6}$$

To get an analytical estimate of the field, we assume a linear and uniform magnetic material. The magnetic flux at the pole tip and the MMF at saturation can then be found by increasing ϕ_{tip} up to the point where $B_{\text{yoke}} = B_{\text{sat}}$ (2.1 T for CoNiFe).

The transverse magnetic flux density at the center of the undulator is reduced by fringing in the axial direction and can be significantly less than the flux density in the cross section of the yoke. The magnetic field of a standard (Design 2) undulator including 2D fringing was analyzed by Poole *et al.* and is given by

$$B_{\text{peak}} = \frac{\phi_{\text{tip}}}{W_y T_y} \frac{1}{\cosh(\xi)} \left(\frac{1 - \sinh(\xi)/[3\sinh(3\xi)]}{1 - \sinh(\xi)/[3\sinh(\xi)]} \right), \tag{7}$$

where $\xi = \pi g/\lambda_u$ [22].

Figure 5 shows the magnetic flux density of the undulator (Design 2) plotted at saturation using Eqs. (5) and (7), varying the undulator period and gap. When all geometric parameters are scaled together, the peak magnetic flux density remains constant. To verify the analytical scaling law, a variety of undulator geometries were simulated using the 2D FEM magnetostatic package in COMSOL MULTIPHYSICS with a nonlinear CoNiFe material model derived from vibrating sample magnetometry studies of $Ni_{80}Fe_{20}$ [12] scaled to the saturation magnetization and initial permeability described in Osaka *et al.* [13].

Analytical results approximate the simulated fields well while $1 \leq \lambda_u/g \leq 8$. For large ratios of period to gap, the

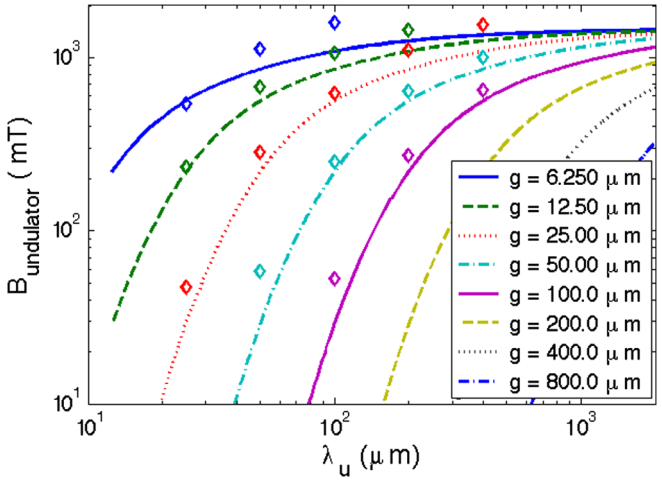

FIG. 5. Plot showing the scaling of the transverse magnetic flux density in the center of the undulator vs gap and period. Values of $L_y = \lambda_u/4$, $W_y = \lambda_u/4$, and $B_{\text{sat}} = 2.1$ T are used. Lines denote calculations and diamonds denote simulations.

undulator tip curvature focuses the field and using $\phi_{\text{tip}}/W_y T_y$ as the flux density at the tip is inadequate. For small ratios of period to gap, longer fringing paths across the window that were neglected become relevant and $\mathcal{R}_{\text{window}}$ is inadequate.

Figure 6 shows the MMF in Amp-turn required to generate 1 T for many different geometries. Peak transduction of electrical current to magnetic field is found across wide bands of period lengths centered at $\lambda_u/g \approx 4$ and is approximately 0.528 A-turn/T/μm $\times$ λ_u [μm].

The maximum MMF that can be generated for each period of the undulator is limited by the maximum allowed current density through the coil before the maximum operating temperature is reached. The maximum operating temperature of the undulator will be reached when either the magnetic material passes the Curie temperature, the

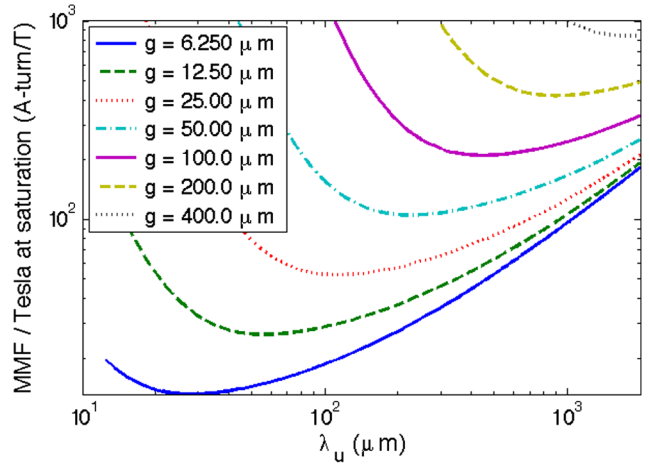

FIG. 6. Plot showing the ratio of the MMF required to saturate the magnetic yoke, normalized to 1 T, for a variety of undulator geometries.

internal stress of the magnetic material increases significantly due to annealing, or the polymer used to isolate the windings from the magnetic yoke decomposes. The curie temperature of $Co_{65}Ni_{12}Fe_{23}$ is typically in excess of 800°C [23]. The internal stress of magnetic alloys containing Ni and Fe anneal to high stress in excess of 250°C and the polymer SU-8 decomposes in vacuum at 280°C, setting a maximum operating temperature of 250°C.

Heat transport from the electromagnet through the substrate is limited by the thermal conductivity of Si to 65 W/cm^2/°C for a 200 μm thick substrate. At 10 kW/cm^2, 150°C of the thermal budget is consumed in a 200 μm Si substrate. The thickness of the bottom and top winding layers can be increased to improve heat transport and reduce Joule heating in the electromagnet using a damascene and through-mold electroforming process, respectively, but the cross section of the vias is limited by the available space between the magnetic yokes. Figure 7 shows the maximum MMF that can be generated for different uniformly scaled geometries dissipating 10 kW/cm^2.

As an example, let us consider a $\lambda_u = 100$ μm, $g = 25$ μm undulator with a 50 μm thick yoke, saturated with 160 A-turns of MMF. Assuming a 32 turn 0.8 Ω coil, we have J $= 2.5 \times 10^{10}$ A/m^2 winding current density, and each period of the undulator will dissipate 5 W. The base of the 200 μm thick substrate needs to be maintained at a temperature below -143°C to keep the undulator from exceeding 250°C. This undulator should be capable of operation when cryogenically cooled by liquid nitrogen. To improve the thermal performance of the undulator, we can reduce the electromagnet yoke thickness to match the size of the gap between the poles. If a 25 μm thick yoke is used, the base of the substrate must be kept below 41°C and the undulator can operate at room temperature.

The optimal design for the undulator electromagnet is obtained as a compromise between (i) reducing the length of the racetrack yoke to minimize the fringing flux losses to reduce the required MMF for a given field and

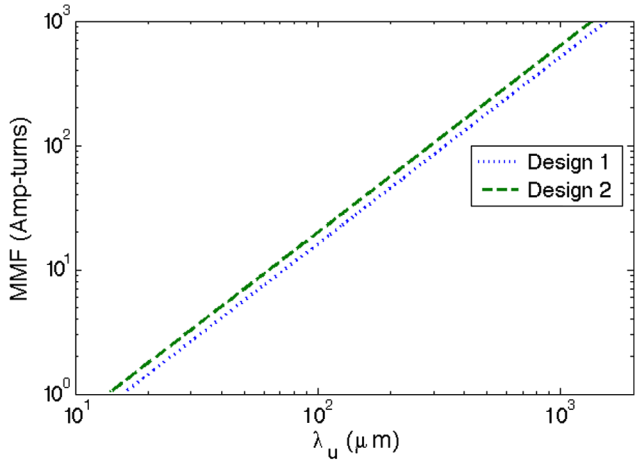

FIG. 7. Plot showing the maximum MMF that can be generated by a 32 turn coil dissipating 10 kW/cm^2.

(ii) increasing the winding cross section to reduce the current density and improve heat transport.

C. Optimization of undulator geometry for higher field

Another design option is to reduce the undulator magnetic gap width below $\lambda_u/4$. This causes the field down the undulator axis to deviate from sinusoidal uniformity, radiating power into higher order harmonics. This deviation can be corrected by shaping the magnetic pole tips. Increasing the radius of curvature of the poles slightly reduces the peak field, but also reduces the contribution of higher order (odd) harmonics in the magnetic field (Fig. 8). Increasing the radius of curvature from 12.5 to 32 μm reduces the third harmonic from 11.5% of the total spectral content to 4.6% and increases the peak of the fundamental harmonic by 7%.

For periods longer than 100 μm, tapering the yoke from a wide back to a $\lambda_u/4$ width pole reduces the magnetic reluctance (see Fig. 3) and spreads out the flux at the back corners of the yoke where the undulator first saturates. 2D nonlinear magnetostatic FEM simulations show that a $\lambda_u =$ 400 μm undulator with yoke tapering and a 50 μm wide magnetic gap produces a saturated peak field of 1500 mT, 45% greater than the untapered yoke. As the undulator period is scaled down, this optimization becomes unfeasible due to the space requirements for the electromagnet winding vias. Table I lists the peak magnetic flux density achieved with a variety of optimized undulator geometries.

The strength of the coupling between the radiation and the relativistic beam is related to the normalized undulator parameter, K,

$$K = \frac{eB_{\text{peak}}\lambda_u}{2\sqrt{2}\pi m_e c}, \tag{8}$$

where e is the charge of an electron, B_{peak} is the peak on-axis transverse magnetic field, λ_u is the undulator period, m_e is the electron mass, and c is the speed of light. The achievable undulator parameter in the range of $\lambda_u = 25\,\mu$m to $\lambda_u = 1$ mm scales between $K = 9\times10^{-4}$ and $K = 0.1$. This is comparable with the shortest period undulators discussed in recent literature, $K = 0.03$ for a 706 μm hybrid permanent micropole undulator [7], $K = 0.4$ for a $\lambda_u = 5$ mm permanent magnet undulator [24], and $K = 0.2$ for a $\lambda_u = 3.8$ mm superconducting undulator [25].

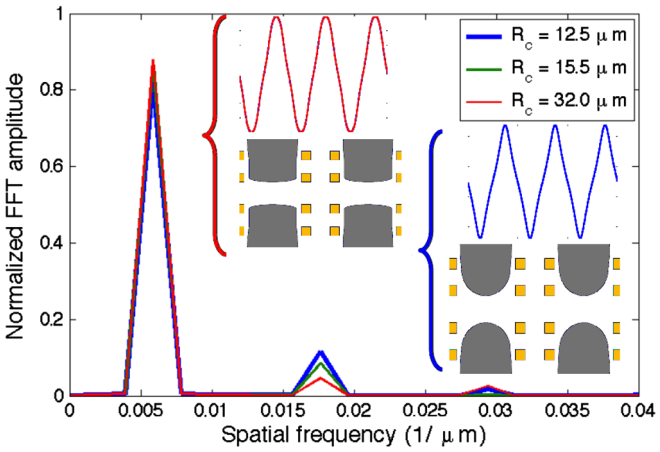

FIG. 8. Plot of the spatial harmonics of the undulator field in Design 2 with $\lambda_u = 100$ μm and $g = 12.5$ μm for several pole tip curvature radii. Data was taken from 2D magnetostatic FEM simulations.

TABLE I. Optimized undulator geometries using Design 2.

λ_u	Undulator gap	B_{peak}	K
25 μm	6.25 μm	540 mT	8.9×10^{-4}
25 μm	12.5 μm	230 mT	3.8×10^{-4}
100 μm	25 μm	727 mT	4.8×10^{-3}
100 μm	50 μm	334 mT	2.2×10^{-3}
400 μm	50 μm	1500 mT	4.0×10^{-2}
400 μm	100 μm	970 mT	2.6×10^{-2}

D. Magnetic field uniformity

The low K value of these undulators implies that magnetic field nonuniformity has a relatively small effect on the undulator resonance condition. However, beam position and focusing will be more sensitive to the magnetic field profile because the electron beam occupies much of the space between the magnetic pole tips. 3D magnetostatic FEM simulations of the field in a 100 μm period, 50 μm $\times$ 50 μm gap undulator were performed with COMSOL MULTIPHYSICS to visualize the transverse behavior of the field. Figures 9 and 10 show the transverse magnetic flux density at different positions in the undulator.

The z dependence of the magnetic field seen in both designs is explained by the fact that out-of-plane magnetic fringing reduces the transverse magnetic flux density away from the center of the undulator. Conversely, in the undulator plane (along the y direction), the magnetic flux is larger as we approach the magnetic flux sources. This effect is more pronounced in Design 1, where the flux source is only on one side (see Fig. 10).

In order to estimate the magnitude of the magnetic field errors in this undulator, we observe from Eq. (7) that the on-axis magnetic field varies inversely with the thickness of the yoke. The precise thickness of binary and trinary magnetic alloys is difficult to control across a patterned feature. A typical random variation in the thickness of the undulator yoke with $\sigma_t = 0.01T_y$ corresponds to a $\sigma_{B,t} = 0.01B_u$ variation in the undulator field.

Nonuniformity in the photolithography exposure tool dose ($< 1\%$ for modern projection and 1.5% for contact lithography tools) will cause variation in the critical dimensions of the yoke. Using the lumped parameter model for optical lithography [26] and assuming a high-contrast negative-tone photoresist and features that are larger than the critical dimension defined in Eq. (2),

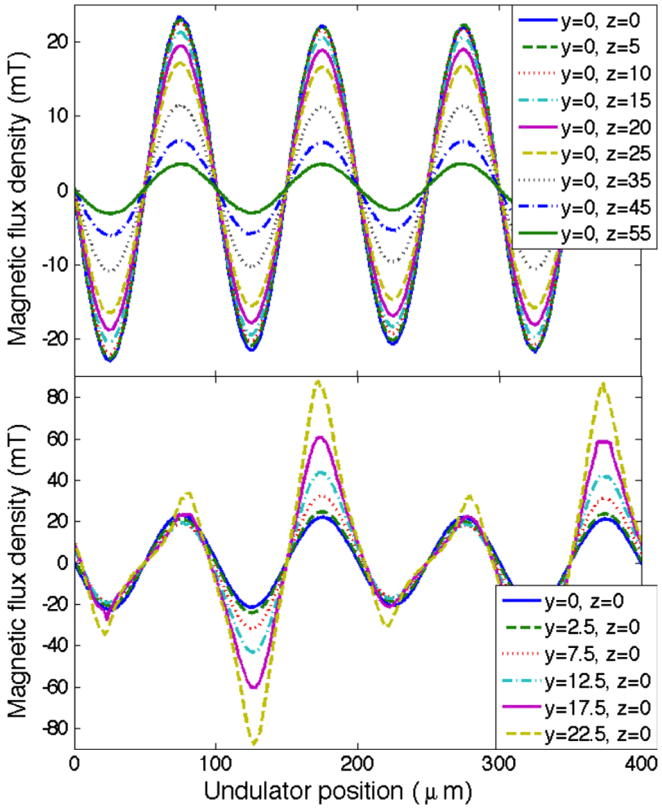

FIG. 9. Transverse magnetic flux density at different positions for Design 1 with $\lambda_u = 100$ μm and $g = 50$ μm. The plot spans 5 of 7 periods of an undulator with $y = z = 0$ μm at the center.

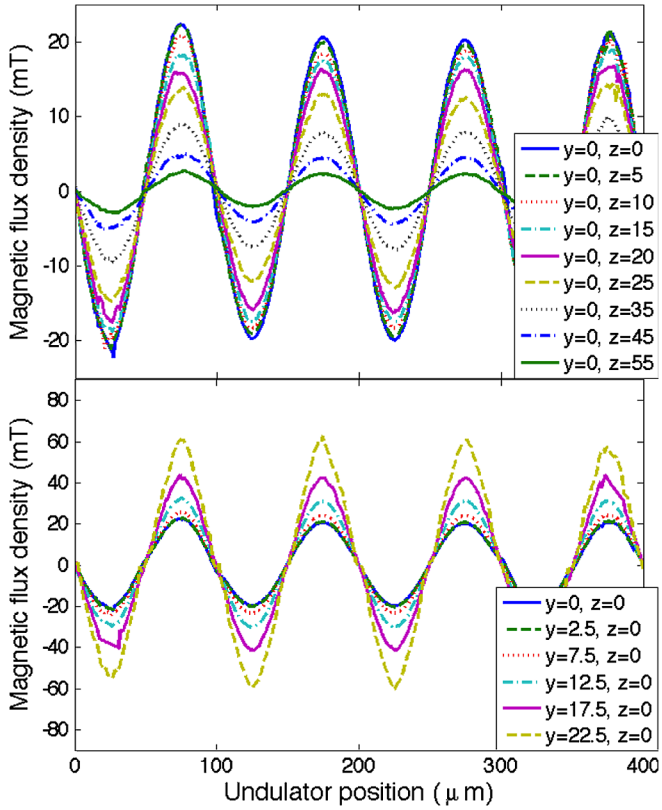

FIG. 10. Transverse magnetic flux density at different positions for Design 2 with $\lambda_u = 100$ μm and $g = 50$ μm. The plot spans 5 of 7 periods of an undulator with $y = z = 0$ μm at the center.

a $\sigma_I = 0.01 I_0$ variation in exposure dose will result in approximately a $\sigma_{CD} = 0.01 b_{\text{crit}}$ critical dimension variation. For a 100 μm thick electromagnet yoke electroplating mold, the undulator gap would then vary by $\sigma_g = 60$ nm. A Taylor expansion to first order of terms containing the gap in Eq. (7), $\xi = \pi g/\lambda_u$, at $g/\lambda_u = 1/2$ shows that the magnetic field varies with $B_u \propto 1.05 - 0.525\xi$. A $\sigma_g = 60$ nm uncorrelated variation in the gap of a $\lambda_u = 100$ μm, $g = 50$ μm undulator and a $\lambda_u = 400$ μm, $g = 100$ μm undulator will result in a $\sigma_{B,g} = 0.005 B_u$ and $\sigma_{B,g} = 0.0004 B_u$ variation in undulator field, respectively.

The total effect of these uncorrelated transverse field errors on the undulator phase matching condition, defined in Eq. (1), will be limited by the small K of the undulator. A $\sigma_B = 0.011 B_u$ total variation in the transverse field intensity with $K = 0.003$ will result in a 1×10^{-7} rms error in the phase matching condition of a $\lambda_u = 100$ μm undulator.

Electrically tuning individual undulator electromagnets can mitigate these errors. For Design 1, Hopkins analysis neglecting fringing yields a tuning range from $B = 0$ to B_{peak}. For Design 2, the full tuning range can be achieved when the yoke is unconnected between undulator periods. When the yoke reluctance between periods is much less than $\mathcal{R}_{\text{total},2}$ and there are many periods, however, tuning range approaches zero.

III. UNDULATOR FABRICATION

The fabrication process is based on a microscale magnetic actuator process [12] and uses planar batch-fabrication processes that are well established in the MEMS community. These processes regularly yield thousands of MEMS devices per wafer. The details of the microsolenoidal electromagnet fabrication process (Fig. 11) are as follows.

(1) The pattern for the bottom coil windings is photolithographically defined on a high-resistivity silicon wafer using a 5 μm thick sacrificial high-aspect-ratio negative-tone photoresist (KMPR 1007, Microchem Corp., Newton, MA). Using this soft mask, 10 μm trenches are anisotropically etched in the silicon wafer using the Bosch process [27] with a deep reactive ion etcher (SLR-770, Plasma-Therm, St. Petersburg, FL). The photoresist is removed in an organic photoresist stripper (ALEG-380, J. T. Baker, Phillipsburg, NJ) and the wafer surface is cleaned in an O_2 plasma (Matrix 105 Plasma Stripper, Matrix Integrated Systems, Richmond, CA).

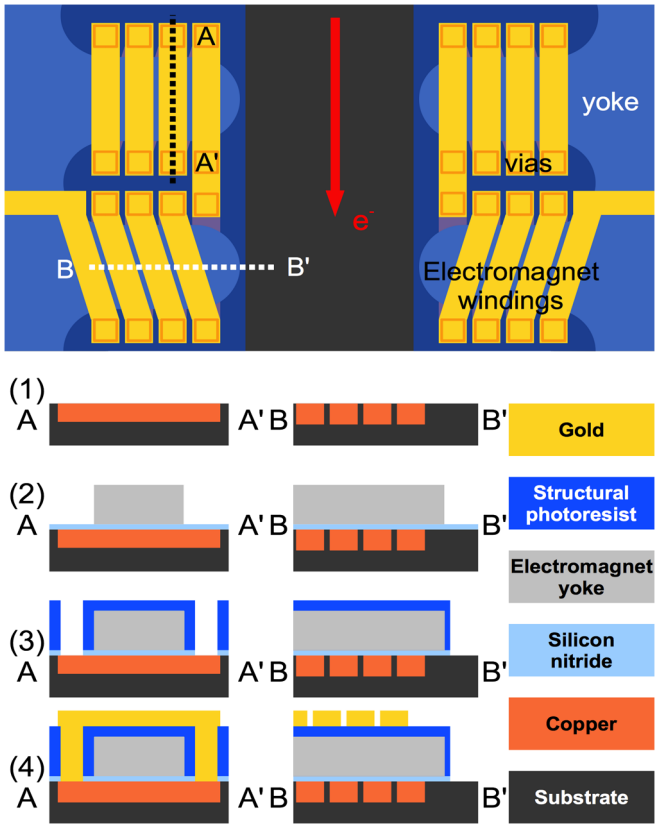

FIG. 11. Microelectromagnet device fabrication process. Film thicknesses are not to scale.

A 100 nm insulating layer of silicon nitride is deposited by inductively coupled plasma enhanced chemical vapor deposition (STS MESC Multiplex CVD, SPTS Technologies Limited, Newport, United Kingdom) to isolate the bottom windings from the silicon substrate. An electroforming seed is deposited on the surface of the silicon nitride by rf sputtering with a 20 kV DC bias (CVC 601, Consolidated Vacuum Corporation (was CVC, now VEECO), Plainview, New York). DC bias is necessary for adequate coverage over the 10 μm wafer topology. The seed layer consists of 30 nm of titanium to provide adhesion to the substrate, 300 nm of copper to carry the electroplating current and compatibility with copper electroplating, and 30 nm of titanium to protect the copper from oxidation. The exposed seed layer is etched to copper in 1% hydrofluoric acid and a 12 μm thick copper film is electroplated from a phosphorized copper anode in a sulfate based solution (Technic Elevate Cu 6320, Technic Inc., Rhode Island). The film is polished back down to the silicon surface (PM5, Logitech Ltd., Glasgow, Scotland), yielding the bottom of the electromagnet winding pattern.

A 300 nm insulating layer of silicon nitride is deposited by inductively coupled plasma enhanced chemical vapor deposition (STS MESC Multiplex CVD, SPTS Technologies Limited, Newport, United Kingdom) to isolate the bottom windings from the conductive magnetic yoke.

(2) An electroforming seed is deposited by sputtering (CVC 601, VEECO, Plainview, New York) on the surface of the silicon nitride. The seed layer consists of 30 nm of titanium to provide adhesion to the substrate, 300 nm of copper to carry the electroplating current and provide a surface compatible with magnetic alloy (NiFe, CoNiFe, or CoNiP) electroplating, and another 30 nm of titanium to protect the copper from oxidation before plating and to provide adhesion between the metal and the electroplating mold.

A 60 μm film of high sidewall-aspect-ratio negative-tone photoresist (KMPR 1025, Microchem Corp., Newton, MA) is photolithographically patterned into the geometry of the magnetic yoke. The exposed seed layer is etched to copper in 1% hydrofluoric acid, and the magnetic alloy that forms the electromagnet yoke is electroplated through the mold using the process detailed by Glickman *et al.* [15]. The mold is removed by delamination after soaking 8 hours in heated organic photoresist stripper (ALEG-380, J. T. Baker, Phillipsburg, NJ). The electroplating seed is stripped by consecutive dips in 1% hydrofluoric acid, a mixture of 5% acetic acid and 15% hydrogen peroxide, and 1% hydrofluoric acid. Figure 12 shows an electromagnetic microactuator yoke fabricated with this process.

(3) A 55 μm layer of structural photoresist (SU-8 2025, Microchem Corp., Newton, MA) is spun on the wafer to isolate the conductive magnetic yoke from the top layer of the coil windings. The photoresist is patterned using photolithography to define the coil winding interconnects and the electron-beam path and annealed under vacuum for 8 hours at 230°C.

The silicon nitride covering the copper at the base of the vias is etched with an inductively coupled CF_4 plasma (STS MESC Multiplex AOE, SPTS Technologies Limited, Newport, United Kingdom) to expose the bottom

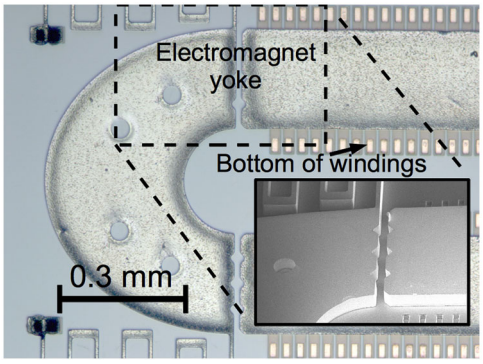

FIG. 12. Photograph of a MEMS microactuator during fabrication demonstrating results of the magnetic yoke electroplating process step. The inset shows a scanning electron micrograph of the pictured microactuator at a 45° angle.

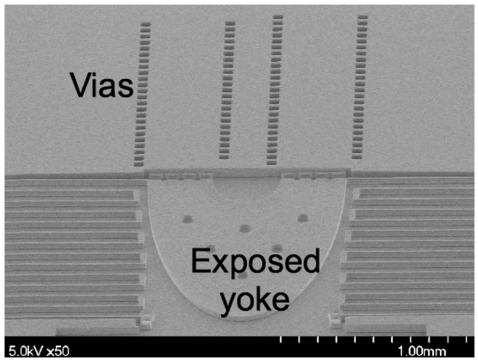

FIG. 13. Scanning electron micrograph taken at 45° showing a MEMS microactuator during fabrication demonstrating results of the via process step.

windings of the coil. Figure 13 shows vias in an electromagnetic microactuator fabricated with this process.

(4) Another electroforming seed is sputtered on the surface (CVC 601, VEECO, Plainview, New York), and a negative-tone photoresist electroplating mold (KMPR 1005, Microchem Corp., Newton, MA) is patterned into the geometry of the top layer of the electromagnet coil windings. Gold is electroplated from a potassium aurocyanide bath (HS434, Technic Inc., Rhode Island) heated to 55°C with strong agitation from a platinized titanium anode through the photopatterned mold to complete the electromagnet coil windings. The mold and electroplating seed are stripped using the process described above, completing the undulator solenoids. Figure 14 shows completed windings in an electromagnetic microactuator fabricated with this process.

Additional processing steps may be necessary for integration with an electron beam line. To carry image current, the gap defined by the thick structural photoresist can be covered with a layer of metal by sputtering or electron-beam evaporation. The windings can be protected from electrical shorts during this metal deposition by either a sacrificial patterned photoresist or a thin film of silicon nitride.

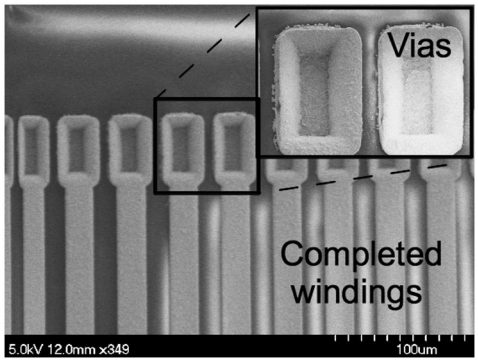

FIG. 14. Scanning electron micrograph of completed windings and vias. The inset shows a more detailed view of the filling of the via.

IV. CHALLENGES

Integrating a microfabricated electromagnetic undulator with a beam line poses several challenges that are not typically encountered with macroscopic permanent magnet, superconducting, or laser undulators. The undulator transverse structure is sub-mm size, and it must be placed inside the vacuum beam line, complicating alignment, electrical interconnects, heat extraction, and beam focusing. Spatial measurements of the actual magnetic field will be complicated by the small undulator gap. Further, the proximity of the undulator surface to the electron bunch influences the beam characteristics.

A. Electromagnet heat dissipation

Heat extraction is a serious challenge when operating electromagnetic undulators under vacuum. Further aggravating heat extraction from the undulator is the reduced cross section of the windings as the undulator period scales down, driving up both current density and coil resistance. Depending on the geometry, the undulator dissipates 100 s of W/cm^2 to 10 s of kW/cm^2 during operation (Fig. 15).

For a saturated 400 μm period undulator with a magnetic gap of 50 μm, 3820 W/cm^2 must be extracted from the undulator to maintain a steady-state temperature. Figure 16 shows the 2D temperature distribution simulated using COMSOL MULTIPHYSICS across a 50 μm tall winding cross section of a $\lambda_u = 400$ μm undulator on a 200 μm thick silicon wafer. Here, the base of the wafer must be held at less than 138°C to keep the structural polymer from exceeding a safe temperature of 250°C. Figure 17 shows the simulated temperature distribution across a 25 μm tall winding cross section of a $\lambda_u = 100$ μm undulator on a

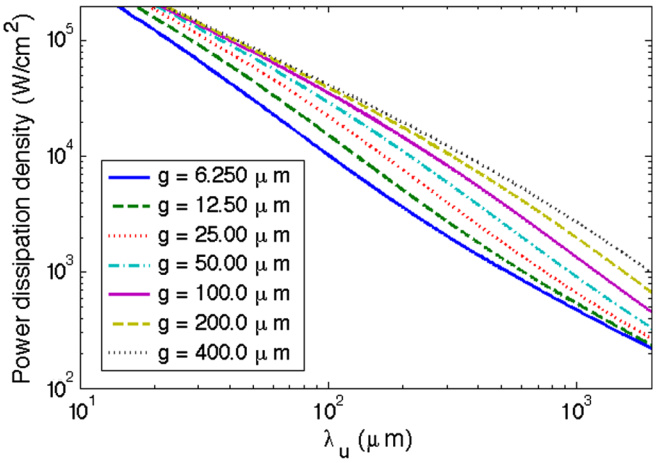

FIG. 15. Plot showing the scaling of the surface power dissipation density generated by the undulator windings at saturation.

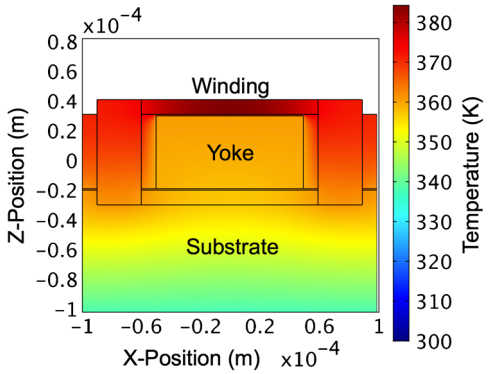

FIG. 16. Temperature distribution simulation (Kelvin) of a $\lambda_u = 400$ μm undulator winding cross section driven with 5 A, producing 1.2 T, fabricated on a 200 μm thick Si wafer.

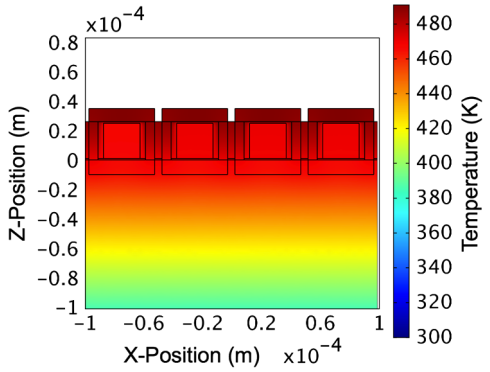

FIG. 17. Temperature distribution simulation (Kelvin) of a $\lambda_u = 100$ μm undulator winding cross section driven with 0.8 A, producing 0.3 T, fabricated on a 200 μm thick Si wafer.

200 μm thick silicon wafer. Here, the base of the wafer must be held at less than 32°C.

For geometries that generate more surface heat density, conductive heat transfer from room temperature is not sufficient to keep the undulator below the structural polymer's decomposition temperature. To address this limitation, the structural polymer may be etched away in O_2 plasma prior to operation, the undulator must be run pulsed, or a circulating liquid or cryogenic cooler may be used to extract heat from the undulator. Given the $\tau = 100$ ns–100 μs response of the undulator inductors, pulsed operation at 1 kHz with a 10% duty cycle would allow all undulator designs to be driven with the substrate held at room temperature. Integrated two-phase microjet impingement cooling [28] is another potential solution to dramatically increase heat transport allowing continuous wave operation without cryogenic cooling.

B. Wakefields

Wakefields generated by the electron beam in sub-mm gaps are significantly stronger than in mm- or cm-scale undulator beam pipes and have the potential to seriously affect the electron-beam energy spread and propagation. There are two main sources for the wakefields, the resistive wall effect and the surface roughness effect.

The resistive wall wakefield is a result of electrical currents induced in the walls of the undulator electron-beam waveguide. These finite currents will excite both transverse magnetic and transverse electric waveguide modes, resulting in longitudinal energy modulation and transverse instability of the electron bunch.

Longitudinal wakefields will induce a significant energy spread in the electron bunch as it travels through the undulator when the length of the electron bunch is comparable to a characteristic distance,

$$s_0 = \left(\frac{g^2}{2Z_0\sigma}\right)^{1/3}, \tag{9}$$

where c is the speed of light, g is the undulator gap (approximating the waveguide cross section as round rather than rectangular), Z_0 is the impedance of free space, and σ is the conductivity of the undulator waveguide walls [29].

Studies by Bane *et al.* showed that a rectangular aluminum beam pipe reduced longitudinal wakefields by 50% compared to an equivalent sized round copper beam pipe [30]. An aluminum covered rectangular beam pipe is compatible with the fabrication process proposed here, and the wakefield effects for this configuration are calculated below. A $g = 100$ μm undulator with an aluminum covered waveguide has a characteristic distance $s_0 = 724$ nm and a loss factor of $k_z = 0.1$ MV/pC/m. The longitudinal energy modulation of a of a 750 A_{peak} 100 pC electron bunch by short-range resistive wall wakefields were calculated using the GENESIS module Genwake for a variety of undulator gap sizes and plotted in Fig. 18.

The other contribution to the undulator wakefield is due to the boundary conditions on the electric field induced by

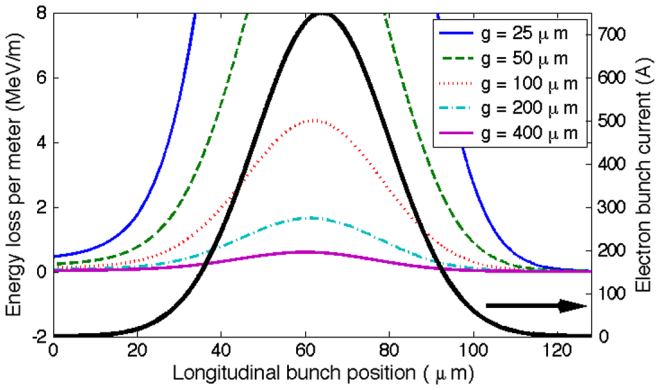

FIG. 18. Resistive wall component of the longitudinal wakefield for a 750 A_{peak} 100 pC Gaussian electron bunch between two parallel aluminum plates separated by g.

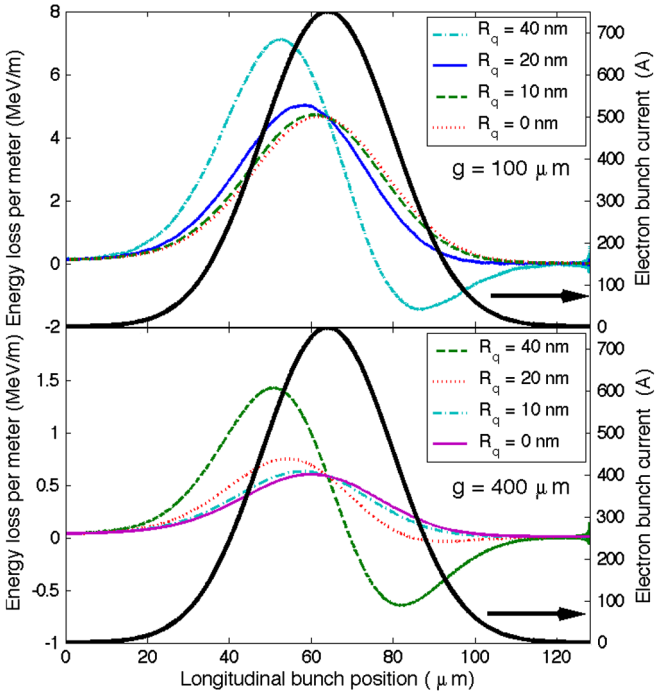

FIG. 19. Longitudinal wakefield for a 100 pC Gaussian electron bunch between two parallel aluminum plates separated by $g = 100$ μm (top) and $g = 400$ μm (bottom).

a rough waveguide wall. This field distortion will impact the energy of subsequent electrons in the bunch with an inductive load on the electron beam [31]. To illustrate this effect, surface roughness wakefields were calculated using the GENESIS module Genwake for an aluminum-coated $g = 100$ μm and $g = 400$ μm waveguide with a variety of surface roughnesses, R_q, and shown in Fig. 19.

The surface morphology of evaporated or sputtered metal films is typically characterized by nm-scale surface roughness that follows the underlying topology. The proposed microundulator fabrication process uses SU-8 polymer patterned by UV photolithography to define the sidewall topology. The sidewall of these SU-8 features has a surface roughness below the measurement capabilities (~ 5 nm) of the scanning electron microscopes used in this work (S-4700, Hitachi Instruments, Inc., San Jose, CA). Tapping mode atomic force microscope measurements have been reported with $R_q \sim 4$ nm_{rms} sidewall surface roughness over a correlation length of 46 nm for proton beam patterned SU-8 [32] and $R_q \sim 4$ nm_{rms} sidewall surface roughness without a reported correlation length for UV-patterned SU-8 [33]. These values are strongly affected by fabrication process conditions, especially the temperature and duration of subsequent anneal bakes and the temperature, duration, and chemistry of subsequent plasma etching steps. Scanning tip profile measurements of SU-8 films during the proposed fabrication process have shown surface roughness ranging from $R_q \sim 1$ nm_{rms} to

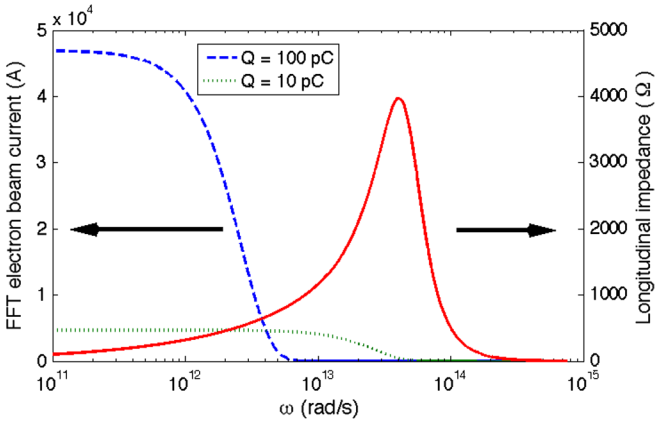

FIG. 20. Spectral distribution of a 750 A_{peak} 10 pC and 100 pC Gaussian electron bunch (dashed) and the resistive wall impedance per unit length for a $g = 100$ μm aluminum waveguide (solid).

$R_q \sim 100$ nm_{rms}, depending on the exposure of the SU-8 to fabrication process conditions.

Because the FEL instability requires that the energy bandwidth in an FEL slice of the electron pulse be less than the Pierce parameter, the energy chirp imparted by wakefields can prevent the microundulator from operating as a FEL [34]. Taking the parameters from the high-gain soft-x-ray FEL amplifier example below, $E = 210$ MeV, $L_g = 53$ cm, $L_c = 1.5$ μm, and $\rho = 4.5 \times 10^{-5}$, the induced energy spread across a FEL slice must be less than ~ 18 keV/m for FEL operation.

In order to further mitigate the longitudinal energy modulation by wakefields, one needs to reduce the amplitude of the electron distribution or minimize the overlap of the spectral components of the beam longitudinal distribution with the impedance response of the structure. One possibility is to reduce the electron bunch charge and length. This wakefield will be reduced approximately in proportion with the reduction in charge, however, submicron bunch lengths may become comparable to the slippage length in the undulator, halting the FEL process. Figure 20 demonstrates the overlap between Fourier transformed $\sigma = 1.6$ μm and $\sigma = 16$ μm Gaussian electron bunches with the same 750 A current, and a $g = 100$ μm rectangular waveguide wake function ([35], Eq. 2.75).

Bane *et al.* suggested that vanishingly small periodic fins in a rectangular waveguide beam pipe would shift the resonant frequency of the cavities between fins beyond the high-frequency cutoff of a finite energy electron beam, $\omega = 2\gamma c/g$ ([36], footnote 17). This analysis was carried out to study surface roughness wakefields, but hints at an interesting strategy to mitigate the effects of Fhod for eliminating unwanted propagating modes in microwave waveguides. Neglecting higher order modes, additional wakefields caused by the waveguide discontinuities, and the evanescent fields in the waveguide stop bands, 15 μm

fins spaced 15 μm apart in a 100 μm wide waveguide might reduce the resistive wall wakefield.

C. Electron-beam induced heating

Energy dissipation in the undulator waveguide by longitudinal wakefields will also cause Joule heating, further complicating thermal management of the undulator.

A 116 MeV electron beam with continuous 1 mA electron current will dissipate 200 W in 5 cm of a $g = 100$ μm undulator waveguide. Wakefield-induced Joule heating will dissipate 334 μJ per shot into each meter of undulator length for a 100 pC bunch in a $g = 100$ μm, $R_q = 10$ nm aluminum-coated undulator waveguide due to the wakefields shown in Fig. 19. At a repetition rate of 1 MHz, wakefields will dissipate <1 kW/cm^2 in the waveguide.

The total of all electron induced heat loads is less than the expected electromagnet dissipation at saturation.

D. Other magnetic fields

The undulator also cannot be placed near macroscopic magnetic electron-focusing optics. Because the magnetic yokes of the device are operated near saturation magnetization, strong external magnetic fields can perturb the magnetic flux sources. In the short term, either macroscopic long focal length magnetostatic focusing optics external to the beam line or electrostatic focusing optics placed within the beam line must be used. In the long term, microfabricated magnetic quadrupoles can be developed to focus the beam.

E. Magnetic measurements

Directly measuring the microscale magnetic field is challenging because the undulator gap is smaller than typical Hall-effect probes, GMR probes, and the wires used in present pulsed-wire undulator characterization [37]. The micropole undulators built by Tatchyn *et al.* were characterized with a novel moving wire measurement for magnetic gaps down to 250 μm [38]. Tatchyn's measurement technique may be scalable to 100 μm gaps, but maintaining μm-scale alignment of the wire as it moves down the cm-scale length of the undulator will be difficult. 25 μm AWG56 BeCu wire and a high-resolution laser doppler vibrometer could be used to extend pulsed-wire testing of undulators down to 100 μm gaps.

For smaller gaps, traditional undulator field characterization methods do not scale and other options such as magnetic force microscopy (MFM) testing or integrated test structures must be used. Such test structures could include patterned magnetoresistive or magneto-optical imaging films integrated in the gap of the undulators to provide direct empirical verification of the field distribution. Sub-10 nm Fe/Cr/Fe trilayer films exhibit a ~40% change in conductivity under 1.3 T applied field at room temperature [39]. Magneto-optical imaging films such as lead- and bismuth-substituted yttrium iron garnet have reported Faraday rotation of 1.85° μm^{-1} for 633 nm light at 295 K [40] and have been prepared as 0.2 wt % concentration nanoparticle solutions with Verdet constants up to 0.03° T^{-1} μm^{-1} for 1.3 μm light at room temperature [41].

V. UNDULATOR RADIATION SOURCE WITH A HIGH AVERAGE CURRENT BEAM

In the last part of this paper we give three examples of possible applications of these new microundulators.

The first example takes advantage of the relatively low power requirements of an electromagnetic microundulator. Competitive approaches to ultrashort wavelength undulators are all based on high power laser pulses which typically have limited repetition rates (<1 kHz). In fact, it is common to invoke complex designs involving recirculating cavities and multi-interaction schemes to get a high average photon yield with a laser based source [42]. Conversely, only a few amps of current are required to drive the electromagnetic microundulator, and it is practical to apply current continuously to the microcoils and have the magnetic field on at all times. It is then natural to couple this undulator with an electron beam from a cw or high duty cycle electron accelerator.

As an example, we consider injecting a 1 mA 116 MeV beam with parameters typical of proposed Energy Recovery Linacs [43] into a microundulator with 400 μm period, 100 μm gap, and 18 cm total length. The magnetic field of the microundulator in this case can be as high as 1.0 T. The resonant wavelength for this case is $\lambda_r = 3.9$ nm. Assuming the undulator natural focusing is equal in the two planes, which can be obtained by properly shaping the magnetic poles, the undulator beta function is

$$\beta^\star = \frac{\sqrt{2}\gamma\lambda_u}{K2\pi}. \tag{10}$$

Because of the small value of K, this only provides weak focusing. In principle, strong focusing could be added to the microundulator. But this would require a careful magnetic design because the yoke operates very close to saturation and nonlinear effects may take place. The total undulator length is then set by the distance of the upstream optics required to focus the beam to a rms beam size small enough to fit the beam through the undulator. For the sake of discussion, we shall require $\sigma_0 < 20$ μm to minimize the portion of the beam incident on the undulator poles (0.1%, or ~100 W). Assuming a normalized transverse emittance of $\epsilon_n = 1$ mm mrad, we can estimate the undulator length $L_u = 2\sigma_0^2\gamma/\epsilon_n \cong 18$ cm.

The total number of photons produced can be estimated using the fact that each electron traversing the undulator will emit $(\pi/3)\alpha K^2$ photons per undulator period in a narrow cone with half-width $\sqrt{\lambda_r/(N_u\lambda_u)} = 0.1$ mrad. The number of photons per second is 3×10^{13} s^{-1}. This photon flux is larger than the state-of-the-art in advanced multi-interaction inverse Compton scattering schemes.

TABLE II. Parameters of a high-average-power soft x-ray source based on a $\lambda_u = 400$ μm MEMS undulator.

E-beam energy	116 MeV
E-beam current	1 mA
Beam emittance	1 mm mrad
Undulator period	400 μm
Undulator gap	100 μm
Peak magnetic field	1.0 T
K (rms)	0.026
N_u	450
Undulator length	18 cm
λ_r	3.9 nm
E_r	319 eV
Average radiation power	0.8 mW
Total photon flux	10^{13} s^{-1}

TABLE III. Parameters of a high-gain soft x-ray FEL amplifier based on a 400 μm MEMS undulator.

E-beam energy	210 MeV
E-beam peak current	750 A
Beam emittance	0.05 mm mrad
Undulator period	400 μm
Undulator gap	100 μm
Peak magnetic field	1.0 T
K (rms)	0.026
N_u	20 000
Undulator length	8 m
λ_r	1.2 nm
E_r	1 keV
Peak radiation power	6.7 MW
Peak photon flux	10^{22} s^{-1}

Another important advantage of this scheme is the spectral brightness. The bandwidth of the radiation could be affected by various factors, such as beam energy spread and emittance. The contribution to the bandwidth due to the undulator itself could be very narrow ($< 0.1\%$). This is not easily achieved in ICS sources where many factors, such as the laser bandwidth or diffraction effects in the focusing geometry, come into play in broadening the spectrum of the generated x rays [44]. The parameters of this example are listed in Table II.

The main problem limiting the obtainable x-ray flux using the microundulator is the small normalized vector potential K. An interesting possibility to increase the number of photons produced is to substantially decrease undulator gap, increasing the peak magnetic field. In this case, wakefields will broaden the radiation and higher (odd) harmonics appear in the undulator spectrum because the magnetic field on the undulator axis is no longer sinusoidal. Nevertheless, the number of photons generated by the beam can be significantly larger.

Even with this preliminary design it is interesting to note that the microundulator opens the possibility of production of nearly monochromatic short wavelength radiation by relatively low energy electron beams without the need for expensive and bulky high-average-power laser systems.

VI. HIGH-GAIN SOFT X-RAY FEL AMPLIFIER

The second example that we analyze is the possibility of using an ultrahigh-brightness beam in conjunction with the microundulator. This is a very exciting case, since the energy requirements to access high-gain FEL amplification and production of coherent radiation at short wavelength will be strongly reduced, bringing a significant advantage in terms of size and cost for a x-ray laser. While the potential of this device is exciting, wakefields will significantly impact the FEL process, requiring new strategies to mitigate these effects before a micro-FEL can be realized.

We consider an example where the microundulator period is 400 μm, gap is 100 μm, and produces a magnetic field amplitude of 1 T. Assuming an input beam energy of 210 MeV, the resonant wavelength of the system is 1.2 nm. The matched beam size for a 0.05 mm mrad normalized emittance beam is 13 μm. It is straightforward to calculate the 1D FEL parameter $\rho = 4.5 \times 10^{-5}$. The 1D gain length of the system is 41 cm and taking into account the 3D effects using Ming Xie's fitting formulas [45] we get 53 cm gain length. In particular, this could be attractive to a variety of FEL test facilities in the 200–300 MeV energy range (SPARC, PSI, SDL) which have already demonstrated kA-class beams and sub-mm-mrad emittance. With some improvements to the beam brightness, it could be possible for these facilities to achieve the parameters used in our FEL simulation, which are reported in Table III.

Exponential amplification of the undulator radiation was simulated with the 3D FEL code GENESIS [46] including in-slice longitudinal space charge effects without wakefields and with resistive wall and surface roughness wakefields. Wakefields were calculated using the GENESIS module Genwake assuming a $g = 100$ μm aluminum covered waveguide with 10 nm surface roughness. Figure 21 shows the power output averaged across the 100 pC electron

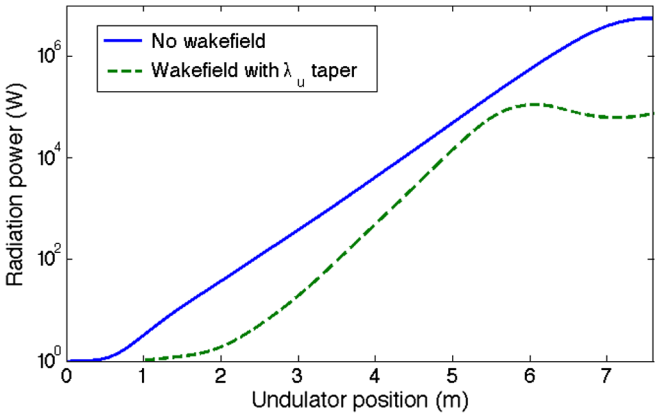

FIG. 21. 3D FEL simulation of the average microundulator radiation power across the electron bunch with and without longitudinal wakefields.

bunch from the beginning of the undulator to the saturation regime.

Without wakefields, we can extract a gain length for the FEL of 0.51 m and estimate 5.5 MW of coherent radiation power in 8 m of undulator from the time independent GENESIS simulation. The difference between the simulated gain length and the gain length calculated using Ming Xie's formula is likely due to space charge forces which are included in the GENESIS simulation, but not in Ming Xie's formulas. The space charge term in the FEL growth eigenfunction, σ_{SC}^2/ρ, has a stabilizing effect competing with the FEL instability [47]. This stabilization increases the gain length, affecting the performance of short-period FELs. Preliminary work to obtain a simple fitting formula to including space charge effects has been made in Marcus *et al.* [48], although three-dimensional simulations are still required to self-consistently include the emittance effects.

Wakefields in the small gap of the undulator modulate the electron energy across the electron bunch. The finite electron bandwidth increases the length of the lethargy regime, prevents the FEL instability from developing in FEL slices where the wakefield-induced bandwidth is greater than 18 keV/m, and causes premature FEL saturation. GENESIS simulation shows that these effects increase the FEL gain length to 1.3 m, reduce the average power across the bunch to 110 kW at saturation, and cause FEL saturation after 6 m of undulator. Radiation bandwidth at saturation is 13%.

In practice, a high performance FEL design with a sub-mm gap undulator will require a larger Pierce parameter, shorter gain length, and a waveguide that mitigates the effects of wakefields. A low-emittance ultrahigh current electron beam, such as the 10 s of kA beams reported from laser-wakefield accelerators [49,50], could be an option to reduce the gain length below 10 cm and increase the Pierce parameter beyond 1×10^4. Real improvement in power output would be limited, however, because wakefields scale up with the peak current. A design that directly addresses longitudinal wakefields in the waveguide could include periodic fins to eliminate propagating transverse magnetic modes of the wakefield.

Since the maximum size of substrates and nanofabrication tooling is limited, a power saturated FEL microundulator will involve aligning 10 s of 8+ cm undulator sections with sub-μm accuracy. Harmonic production will be limited due to the very small undulator K value.

These results show potential for surface-micromachined magnetic undulators to couple with high-brightness beams for ultracompact FELs operating in the exponential gain region.

VII. PROOF-OF-PRINCIPLE EXPERIMENT

Finally we present a proof-of-principle experiment aimed at demonstrating the feasibility of coupling a high-brightness electron beam in the small gap of a prototype surface-micromachined 100 μm period microundulator. A 500 period undulator with 100 μm period length (5 cm total length) and 200 mT_{peak} transverse magnetic field will be fabricated in the UCLA Nanoelectronics Research Facility and tested using the ultrasmall emittance beam available at the Pegasus rf photoinjector. The Pegasus beam line is described elsewhere [51]. We report the parameters of the beam in Table IV. Preliminary tests show that the 4 MeV 10 pC electron beam can be focused down to a 18 μm spot size. With 0.1 mm mrad normalized beam emittance, the beta function is 2.5 cm. The goal of the first experiments is detection of spontaneous undulator radiation at 816 nm from the MEMS fabricated undulator. This is a very convenient range in the electromagnetic spectrum, since diagnostics in the visible are very sensitive and easily available. Even though the energy estimated for spontaneous radiation in these conditions will be weak (only few thousands of visible/IR photon generated), we will be able to use intensified CCD cameras with single photon detection capabilities to characterize the radiation.

TABLE IV. Parameters of the test experiment for the micro-undulator at the Pegasus beam line.

E-beam energy	4 MeV
E-beam peak current	100 Amp
Beam emittance	0.1 mm mrad
Undulator period	100 μm
Undulator gap	50 μm
Peak magnetic field	0.2 T
K (rms)	0.003
N_u	500
Undulator length	5 cm
λ_r	816 nm
E_r	1.5 eV

Another feasible experiment will be to use the 800 nm Ti:Sa laser system available in the Pegasus laboratory to microbunch the 4 MeV beam at 800 nm with a seed radiation pulse. This is an application for which micro-undulators might be uniquely suited. Currently, there is no way to efficiently couple a low energy electron beam and an optical or near infrared laser. The period of conventional undulator magnets is too long to tune at the resonance condition and harmonic coupling coefficients quickly decrease in amplitude with increasing harmonic number. This coupling can be used to diagnose and manipulate the longitudinal phase space of low energy beams at the optical scale. Coupling this scheme with recent ideas on longitudinal space charge amplification [52], which naturally works better at lower beam energy, might open a path towards a new kind of radiation source.

VIII. CONCLUSIONS

In this paper, we discuss the idea of using a MEMS fabricated microundulator for advanced light sources. With

the new progress in nanofabrication techniques, it becomes feasible to build electromagnetic undulators with periods in the 10 μm–1 mm range. This period range is presently not covered by other undulator technology and is very attractive since it bridges the gap between traditional permanent-magnet undulators and laser undulators employed in inverse Compton scattering sources.

ACKNOWLEDGMENTS

The authors would like to thank Xiaoxu Wu for her valuable fabrication process development work, the Nanoelectronics Research Facility at the University of California, Los Angeles for use of their extensive fabrication capabilities, and the Nano and Pico Characterization Lab at the California NanoSystems Institute for use of their AFM/MFM instruments. This work was supported in part by the U.S. Defense Advanced Research Projects Agency under Grant No. N66001-12-1-4209.

[1] R. Bonifacio, C. Pellegrini, and L. Narducci, Opt. Commun. **50**, 373 (1984).
[2] R. Schoenlein, W. Leemans, A. Chin, P. Volfbeyn, T. Glover, P. Balling, M. Zolotorev, K. Kim, S. Chattopadhyay, and C. Shank, Science **274**, 236 (1996).
[3] V. Granatstein, W. Destler, and I. Mayergoyz, Appl. Phys. Lett. **47**, 643 (1985).
[4] G. Ramian, L. Elias, and I. Kimel, Nucl. Instrum. Methods Phys. Res., Sect. A **250**, 125 (1986).
[5] K. Paulson, Nucl. Instrum. Methods Phys. Res., Sect. A **296**, 624 (1990).
[6] R. Tatchyn and P. Csonka, Appl. Phys. Lett. **50**, 377 (1987).
[7] R. Tatchyn, A. Toor, J. Hunter, R. Hornady, D. Whelan, G. Westenskow, P. Csonka, T. Cremer, and E. Kallne, J. X-Ray Sci. Technol. **1**, 79 (1989).
[8] R. Tatchyn, P. Csonka, and A. Toor, Rev. Sci. Instrum. **60**, 1796 (1989).
[9] Y. Ding, A. Brachmann, F. Decker, D. Dowell, P. Emma, J. Frisch, S. Gilevich, G. Hays, P. Hering, Z. Huang *et al.*, Phys. Rev. Lett. **102**, 254801 (2009).
[10] D. Arnold and N. Wang, J. Microelectromech. Syst. **18**, 1255 (2009).
[11] T. Plettner, R. L. Byer, C. McGuinness, and P. Hommelho, Phys. Rev. ST Accel. Beams **12**, 101302 (2009).
[12] M. Glickman, J. Harrison, T. Niblock, P. Tseng, and J. Judy, in *Hilton Head 2010*, A Solid-State Sensors, Actuators and Microsystems Workshop (Transducer Research Foundation, Inc., San Diego, 2010), pp. 328–331.
[13] T. Osaka, M. Takai, K. Hayashi, Y. Sogawa, K. Ohashi, Y. Yasue, M. Saito, and K. Yamada, IEEE Trans. Magn. **34**, 1432 (1998).
[14] B. Orlando, R. Hida, R. Cuchet, M. Audoin, B. Viala, D. Pellissier-Tanon, X. Gagnard, and P. Ancey, IEEE Trans. Magn. **42**, 3374 (2006).
[15] M. Glickman, P. Tseng, J. Harrison, I. Goldberg, P. Johnson, P. Smeys, T. Niblock, and J. Judy, in *International Solid-State Sensors, Actuators and Microsystems Conference, 2009* (IEEE, New York, 2009), pp. 248–251.
[16] M. Glickman, P. Tseng, J. Harrison, T. Niblock, I. B. Goldberg, and J. W. Judy, J. Microelectromech. Syst. **20**, 842 (2011).
[17] J. Clarke, *The Science and Technology of Undulators and Wigglers* (Oxford University Press, New York, 2004), Vol. 4.
[18] M. Madou, *Fundamentals of Microfabrication: The Science of Miniaturization* (CRC, Boca Raton, FL, 2002).
[19] W. Flack, S. White, and B. Todd, in *Advances in Resist Technology and Processing XVI Proceedings* (SPIE, Bellingham, WA, 1999), pp. 474–490.
[20] B. Chaudhri, F. Ceyssens, P. De Moor, C. Van Hoof, and R. Puers, J. Micromech. Microeng. **20**, 064006 (2010).
[21] C. Lee and K. Jiang, J. Micromech. Microeng. **18**, 055032 (2008).
[22] M. Poole and R. Walker, Nucl. Instrum. Methods **176**, 487 (1980).
[23] Y. Omata, IEEE Trans. Magn. Jpn. **5**, 17 (1990).
[24] T. Eichner, F. Gruner, S. Becker, M. Fuchs, D. Habs, R. Weingartner, U. Schramm, H. Backe, P. Kunz, and W. Lauth, Phys. Rev. ST Accel. Beams **10**, 082401 (2007).
[25] T. Hezel, B. Krevet, H. O. Moser, J. A. Rossmanith, R. Rossmanith, and T. Schneider, J. Synchrotron Radiat. **5**, 448 (1998).
[26] C. Mack, *Fundamental Principles of Optical Lithography: The Science of Microfabrication* (Wiley-Interscience, Chichester, 2007).
[27] F. Laermer and A. Schilp, Method of Anisotropically Etching Silicon (1996), U.S. Patent 5,501,893.
[28] E. Wang, L. Zhang, L. Jiang, J.-M. Koo, J. Maveety, E. Sanchez, K. Goodson, and T. Kenny, J. Microelectromech. Syst. **13**, 833 (2004).
[29] K. Bane and M. Sands, AIP Conf. Proc. **367**, 131 (1996).
[30] K. Bane, in *The Physics and Applications of High Brightness Electron Beams: Proceedings of the 46th Workshop of the INFN ELOISATRON Project: Erice, Italy, 2005* (World Scientific, Singapore, 2007), Vol. 28, p. 46.
[31] K. Bane, C. Ng, and A. Chao, in *Proceedings of the Particle Accelerator Conference, Vancouver, BC, Canada, 1997* (IEEE, New York, 1997), Vol. 2, pp. 1738–1740.
[32] T. Sum, A. Bettiol, H. Seng, J. Kan, and F. Watt, Appl. Phys. Lett. **85**, 1398 (2004).
[33] R. Zheng, W. Sun, and X. Chen, J. Micromech. Microeng. **20**, 035007 (2010).
[34] K. Bane and G. Stupakov, *Resistive Wall Wakefield in the LCLS Undulator* (United States Department of Energy, Washington, DC, 2005).
[35] A. Chao, A. Chao, and A. Chao, *Physics of Collective Beam Instabilities in High Energy Accelerators* (Wiley, New York, 1993).
[36] K. Bane and G. Stupakov, Phys. Rev. ST Accel. Beams **6**, 024401 (2003).
[37] R. Warren, Nucl. Instrum. Methods Phys. Res., Sect. A **272**, 257 (1988).
[38] R. Tatchyn and P. Csonka, J. Phys. D **20**, 394 (1987).

[39] M. Baibich, J. Broto, A. Fert, F. Nguyen Van Dau, F. Petro, P. Etienne, G. Creuzet, A. Friederich, and J. Chazelas, Phys. Rev. Lett. **61**, 2472 (1988).
[40] P. Hansen, K. Witter, and W. Tolksdorf, Phys. Rev. B **27**, 6608 (1983).
[41] Y. Jeon, J. Lee, J. Oh, J. Lee, and S. Choi, Phys. Status Solidi (a) **201**, 1893 (2004).
[42] I. Jovanovic, M. Shverdin, D. Gibson, and C. Brown, Nucl. Instrum. Methods Phys. Res., Sect. A **578**, 160 (2007).
[43] C. Mayes and G. Hostaetter, in *Proceedings of the International Particle Accelerator Conference, Kyoto, Japan* (ICR, Kyoto, 2010), TUPE098.
[44] J. Rosenzweig and O. Williams, AIP Conf. Proc. **877**, 437 (2006).
[45] M. Xie, Nucl. Instrum. Methods Phys. Res., Sect. A **445**, 59 (2000).
[46] S. Reiche, P. Musumeci, and K. Goldammer, in *Proceedings of the 2007 Particle Accelerator Conference, Albuquerque, New Mexico* (IEEE, New York, 2007), pp. 1269–1271.
[47] J. Murphy, C. Pellegrini, and R. Bonifacio, Opt. Commun. **53**, 197 (1985).
[48] G. Marcus, E. Hemsing, and J. Rosenzweig, Phys. Rev. ST Accel. Beams **14**, 080702 (2011).
[49] C. Geddes, C. Toth, J. Van Tilborg, E. Esarey, C. Schroeder, D. Bruhwiler, C. Nieter, J. Cary, and W. Leemans, Nature (London) **431**, 538 (2004).
[50] C. Geddes, K. Nakamura, G. Plateau, C. Toth, E. Cormier-Michel, E. Esarey, C. Schroeder, J. Cary, and W. Leemans, Phys. Rev. Lett. **100**, 215004 (2008).
[51] J. Moody, P. Musumeci, M. Gutierrez, J. Rosenzweig, and C. Scoby, Phys. Rev. ST Accel. Beams **12**, 070704 (2009).
[52] E. A. Schneidmiller and M. V. Yurkov, Phys. Rev. ST Accel. Beams **13**, 110701 (2010).